07 Aug 2020

Structure and Function of a Flavin-dependent S-monooxygenase from Garlic (Allium Sativum)

Hannah Valentino

Ashley C. Campbell

Jonathan P. Schuermann

Nazneen Sultana

et. al. For a complete list of authors, see https://scholarsmine.mst.edu/chem_facwork/3950

Recommended Citation

H. Valentino et al., "Structure and Function of a Flavin-dependent S-monooxygenase from Garlic (Allium Sativum)," *Journal of Biological Chemistry*, vol. 295, no. 32, pp. 11042 - 11055, Elsevier; American Society for Biochemistry and Molecular Biology, Aug 2020.
The definitive version is available at https://doi.org/10.1074/jbc.ra120.014484

Structure and function of a flavin-dependent S-monooxygenase from garlic (*Allium sativum*)

Received for publication, May 22, 2020, and in revised form, June 7, 2020 Published, Papers in Press, June 11, 2020, DOI 10.1074/jbc.RA120.014484

Hannah Valentino[1,2], Ashley C. Campbell[3], Jonathan P. Schuermann[4], Nazneen Sultana[1], Han G. Nam[1], Sophie LeBlanc[1], John J. Tanner[3,5,*], and Pablo Sobrado[1,2,*]

From the [1]Department of Biochemistry, Virginia Tech, Blacksburg, Virginia, USA, the [2]Center for Drug Discovery, Virginia Tech, Blacksburg, Virginia, USA, the [3]Department of Biochemistry, University of Missouri, Columbia, Missouri, USA, the [4]Northeastern Collaborative Access Team, Department of Chemistry and Chemical Biology, Cornell University, Ithaca, New York, USA, and the [5]Department of Chemistry, University of Missouri, Columbia, Missouri, USA

Edited by Ruma Banerjee

Allicin is a component of the characteristic smell and flavor of garlic (*Allium sativum*). A flavin-containing monooxygenase (FMO) produced by *A. sativum* (AsFMO) was previously proposed to oxidize *S*-allyl-L-cysteine (SAC) to alliin, an allicin precursor. Here, we present a kinetic and structural characterization of AsFMO that suggests a possible contradiction to this proposal. Results of steady-state kinetic analyses revealed that AsFMO exhibited negligible activity with SAC; however, the enzyme was highly active with L-cysteine, *N*-acetyl-L-cysteine, and allyl mercaptan. We found that allyl mercaptan with NADPH was the preferred substrate-cofactor combination. Rapid-reaction kinetic analyses showed that NADPH binds tightly (K_D of ~2 μM) to AsFMO and that the hydride transfer occurs with pro-*R* stereospecificity. We detected the formation of a long-wavelength band when AsFMO was reduced by NADPH, probably representing the formation of a charge-transfer complex. In the absence of substrate, the reduced enzyme, in complex with $NADP^+$, reacted with oxygen and formed an intermediate with a spectrum characteristic of C4a-hydroperoxyflavin, which decays several orders of magnitude more slowly than the k_{cat}. The presence of substrate enhanced C4a-hydroperoxyflavin formation and, upon hydroxylation, oxidation occurred with a rate constant similar to the k_{cat}. The structure of AsFMO complexed with FAD at 2.08-Å resolution features two domains for binding of FAD and NADPH, representative of class B flavin monooxygenases. These biochemical and structural results are consistent with AsFMO being an S-monooxygenase involved in allicin biosynthesis through direct formation of sulfenic acid and not SAC oxidation.

Garlic (*Allium sativum*) is one of the best known and most consumed spices worldwide, serving as a key ingredient in many dishes. In addition to being used for its flavor and aroma, garlic has been utilized as a nutraceutical for thousands of years. Records, dating as far back as 2700 BC in Asia, indicate that garlic was used in remedies for treating skin infections, gastrointestinal diseases, bronchitis, and cardiovascular illness (1). Garlic's distinct taste is due, in part, to the production of organosulfur compounds, specifically allicin (*S*-allyl prop-2-ene-1-sulfinothioate) and its allyl sulfide derivatives, such as diallyl disulfide, diallyl trisulfide, and ajoene. Extensive experimentation has shown that these compounds exhibit numerous health properties, including antimicrobial, anticancer, anti-inflammatory, and cardiovascular benefits (2–8). Agricultural benefits from allicin have also been described, showing potential application in organic farming (9). One of the main issues with using these compounds is that they are very reactive and organosulfur production varies greatly between garlic plants, depending on soil, temperature, season, and other factors, making standardization of allicin production through agricultural means a challenging task (10–12). Therefore, a better understanding of the enzymes involved in this pathway would make it possible to engineer allicin biosynthesis for flavor and medicinal applications.

In garlic, allicin plays a role in the defense mechanism that is initiated after damage to the plant tissue. Radiolabeling studies have led to the proposal that there are two allicin biosynthetic pathways, starting with either L-serine or L-GSH (5, 13, 14). Both pathways involve the incorporation of an allyl donor from an unknown source, ultimately leading to the synthesis of the stable sulfoxide alliin (Scheme 1). In response to plant injury, alliin is hydrolyzed by alliinase into allyl sulfenic acid and pyruvate, with the consecutive nonenzymatic reaction of two allyl sulfenic acids producing allicin. A key enzyme involved in allicin biosynthesis is a flavin-containing monooxygenase (FMO), which has been proposed to convert *S*-allyl-L-cysteine (SAC) into alliin through a chiral sulfoxidation reaction (Scheme 1) (15).

FMOs belong to the large family of flavin-dependent monooxygenases, specifically to the subclass B monooxygenases, which are important players in many biosynthetic pathways due to their ability to oxygenate a range of substrates, including aromatic carbons, ketones, and soft nucleophilic heteroatoms (16, 17). The general reaction of members of this class is divided into reductive and oxidative half-reactions. The reductive half-reaction involves binding of NAD(P)H, hydride transfer to FAD, and formation of the reduced enzyme in complex with $NADP^+$. Retention of $NADP^+$ by the reduced enzyme is important for the oxidative half-reaction, as it is essential for the formation and stabilization of the C4a-hydroxyflavin species, which is the intermediate that performs the hydroxylation of

This article contains supporting information.

*For correspondence: Pablo Sobrado, psobrado@vt.edu; John J. Tanner, tannerjj@missouri.edu.

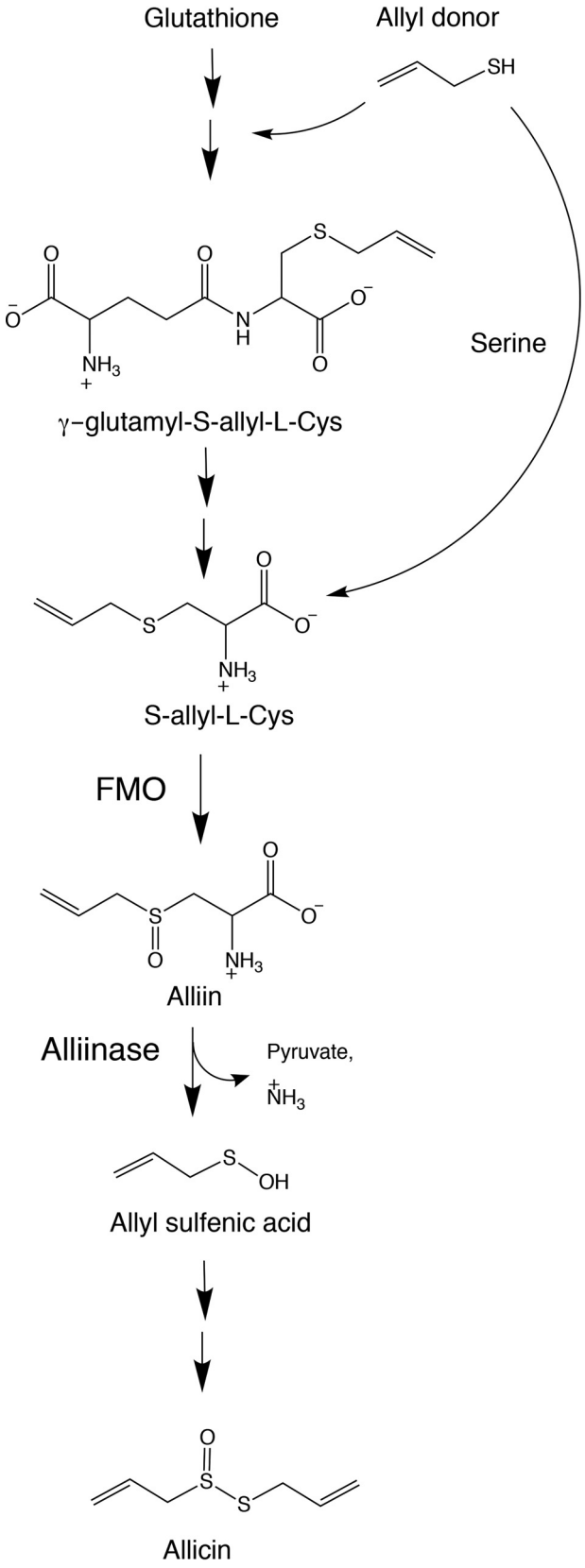

Scheme 1. Generally accepted allicin biosynthetic pathway (5). Feeding studies performed by Granroth have shown serine and GSH to be key metabolites of this process, as they are integrated into SAC (13). AsFMO has been proposed to oxidize SAC, producing alliin, which is subsequently hydrolyzed by alliinase into allyl sulfenic acid and pyruvate. Allyl sulfenic acid then reacts with another allyl sulfenic acid, producing allicin.

the aromatic, N- and S-containing compounds. (18–20). These reactions are highly stereospecific, which makes FMOs attractive targets for industrial applications (21). FMOs from plants contain the largest number of enzymes and have been shown to be involved in cell signaling, defense, and detoxification (22). FMOs from this kingdom are separated into three clades according to sequence homology. Clade I FMOs are involved in plant defense, as represented by the recently characterized enzyme from *Arabidopsis thaliana*, which catalyzes N-hydroxylation of pipecolic acid (23). Clade II includes YUCCA enzymes, which are involved in auxin biosynthesis (24). Clade III can be best described as $FMO_{GS\text{-}OX1\text{-}5}$, which is involved in the S-oxidation of the anticarcinogenic compounds glucosinolates (25). Previous work by Yoshimoto and Saito suggested that the *A. sativum* FMO (AsFMO) and similar FMOs from other *Allium* plants belong to Clade III and are involved in the biosynthesis of *S*-alk(en)yl-L-cysteine sulfoxides, including alliin and similar sulfur compounds, methiin, propiin, and ethiin (14). While there have been some reports of AsFMO activity in yeast cell extracts, as well as *in vivo* activity of similar enzymes (15, 26–28), the isolation and *in vitro* characterization of this enzyme have yet to be accomplished. In this work, we present the biochemical and structural characterization of AsFMO, as well as a detailed understanding of the function of this enzyme, providing biochemical evidence of its role in the biosynthetic pathway for allicin production in plants.

Results

Protein expression and purification

Recombinant AsFMO was initially expressed as an N terminus-His_6 fusion protein; however, this form of the protein was highly insoluble. To overcome this problem, the protein was then expressed as a fusion with His_6-maltose-binding protein (MBP) and purified using immobilized metal affinity chromatography (IMAC). The MBP-AsFMO fusion protein was treated with tobacco etch virus (TEV) protease and the free AsFMO was stable and could be isolated to >95% homogeneity, as determined by SDS-PAGE (Fig. S1). The protein yield was 1.3 ± 0.2 mg protein/1 g of cell pellet. It was determined by MS that the protein contained FAD (data not shown) and ~50% of the protein contained flavin. The absorbance spectrum of bound flavin was very similar to that of free FAD (Fig. S2). The extinction coefficient of FAD bound to AsFMO at pH 7.5 was determined to be 12.8 mM^{-1} cm^{-1} at 450 nm.

Steady-state kinetics

The activity under steady-state conditions was monitored by following oxygen consumption. AsFMO showed an initial velocity of 0.06 ± 0.005 s^{-1} when SAC was used as the substrate, which resembled the background activity with no substrate (Fig. 1*A*). These results were also obtained when the buffer conditions were changed to sodium phosphate pH 7.5 or Tris-Cl pH 8.0. Even when a reaction mixture of 0.5 μM enzyme, 15 mM SAC, and 5 mM NADPH was incubated for 5 h, there were still no observable changes in SAC concentration (Fig. S3*A*).

To identify potential substrates for AsFMO, the allicin biosynthetic pathway and other thiol-containing compounds were

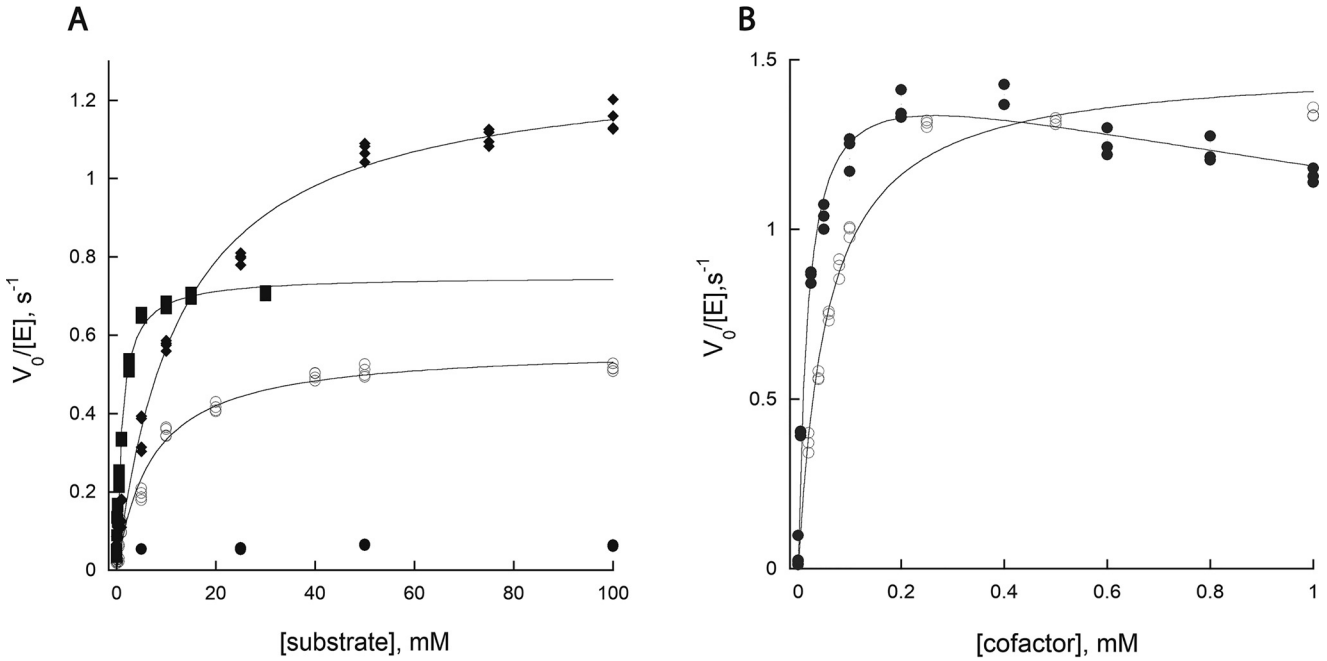

Figure 1. Initial velocity of AsFMO under various conditions. *A*, initial velocity determined by monitoring oxygen consumption by AsFMO in 50 mM HEPES pH 7.5 with increasing concentrations of substrate SAC (●), Cys (♦), NAC (○), and AM (■) in the presence of 0.25 mM NADPH. *B*, initial velocity of AsFMO as a function of NADPH (●) and NADH (○) in the presence of 100 mM Cys.

Table 1
Steady-state kinetic parameters for AsFMO with different substrates, determined by oxygen consumption assay

Variable substrate[a]	Fixed substrate	k_{cat} (s^{-1})	K_m (mM)	k_{cat}/K_m (mM^{-1} s^{-1})	K_i (mM)[b]
AM	NADPH	0.75 ± 0.01	1 ± 0.1	0.75 ± 0.08	N.A.
Cys	NADPH	1.3 ± 0.05	11 ± 0.5	0.11 ± 0.007	N.A.
L-Cysteine	NADH	1.7 ± 0.03	5 ± 0.4	0.34 ± 0.03	N.A.
NAC	NADPH	0.57 ± 0.004	7 ± 0.4	0.08 ± 0.005	N.A.
NADPH	Cys	1.5 ± 0.02	0.019 ± 0.0002	79 ± 1	4 ± 0.2
NADH	Cys	1.5 ± 0.01	0.056 ± 0.0002	27 ± 0.2	N.A.

[a] Conditions were 50 mM HEPES pH 7.5, with fixed concentrations of 0.25 mM NADPH, 0.5 mM NADH, or 150 mM Cys.
[b] N.A., not applicable.

reviewed. *S*-Methyl-L-cysteine, GSH, L-cysteine (Cys), *N*-acetyl-L-cysteine (NAC), allyl mercaptan (AM), thiopropane, thioethane, and thiomethoxide were selected and tested as potential substrates. Of these, Cys, NAC, and AM exhibited significant activity (Fig. 1*A*), whereas the others showed negligible or no activity. We also monitored the levels of Cys and showed that they decreased as a function of time (Fig. S3*B*). The kinetic parameters obtained from the oxygen consumption assays are summarized in Table 1. The results show a 2–3-fold higher k_{cat} value with Cys, compared with AM and NAC; however, the K_m value is 5–10-fold lower for AM, resulting in a 2–9-fold higher k_{cat}/K_m value. AsFMO exhibited a 2–7-fold higher k_{cat}/K_m value with NADPH, compared with NADH, originating from a lower K_m value for NADPH. Substrate inhibition was observed only with excess NADPH, with a K_i value of 4 mM (Fig. 2*B*).

Product formation with Cys

The product of the enzyme reaction with Cys was determined by MS (Fig. S4). Cys was identified in the reaction mixture with an m/z value of 122.027, which matches the values observed for Cys in the control samples. A peak at m/z 241.033 was observed in the reaction mixture, consistent with formation of L-cystine. Control experiments with a L-cystine standard supported this assignment. The peak was present only in the reaction mixture and was not observed in the nonenzyme control (Fig. S4). From these observations, it is likely that AsFMO hydroxylates the thiol group on Cys, forming Cys sulfenic acid. The product then reacts nonenzymatically with excess Cys to form L-cystine (Scheme S1). Sulfenic acid detection was attempted using the derivatization agents 5,5-dimethyl-1,3-cyclohexanedione (dimedone) and *cis*-5-norbornene-endo-2,3-

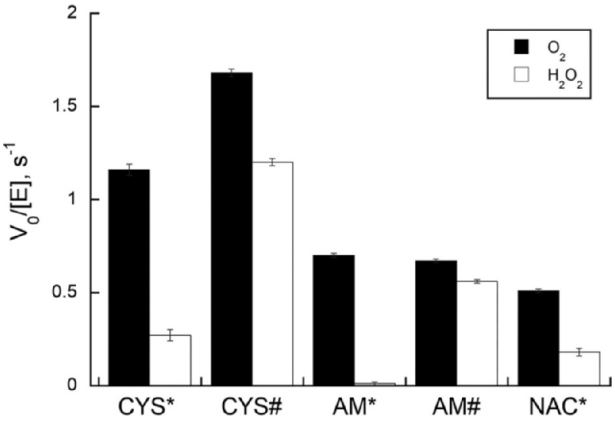

Figure 2. Determination of coupled and uncoupled reactions of AsFMO. The initial velocities of AsFMO were measured by oxygen consumption (*black bars*) and the rate of hydrogen peroxide formation (*white bars*). The final concentrations were 150 mM Cys, 25 mM AM, 150 mM NAC, 0.25 mM NADPH (*), and 0.5 mM NADH (#). The percentages of the uncoupled reaction for each condition were as follows: Cys*, 23 ± 3%; Cys#, 71 ± 2%; AM*, 1 ± 1%; AM#, 84 ± 2%; NAC*, 35 ± 4%.

dicarboxylic acid, with no success (data not shown). It is possible that the reactivity of Cys sulfenic acid with excess free Cys prevented derivatization.

Hydrogen peroxide formation

While FMOs commonly perform hydroxylation reactions, they are also known to produce hydrogen peroxide as part of an unproductive or uncoupled reaction (29–32). This usually occurs very slowly when there is no substrate or when an inhibitor or nonoptimal substrate binds to the active site. If H_2O_2 is produced, it is possible that it will nonenzymatically react with Cys, producing Cys sulfenic acid and, subsequently, L-cystine (33). Therefore, determining the rate of the uncoupled reaction was essential in determining whether the observed activity was enzymatically produced or was a byproduct of uncoupling. This was accomplished by comparing the change in the rate of oxygen consumption of AsFMO in the presence of catalase. Catalase was selected for this experiment because it converts H_2O_2 into water and oxygen, which can be directly measured as a decrease in the initial rate in oxygen consumption assays. By monitoring NADPH oxidation, it was determined that 1 mg/ml catalase did not inhibit the enzyme activity; however, there was a decrease in the activity measured by monitoring oxygen consumption (Fig. S5). The percentage of the enzymatic reaction of Cys, NAC, and AM that was uncoupled with NADPH under saturated conditions (Fig. 2) was much lower than that with NADH, suggesting that NADPH is the preferred cofactor. The reaction with NADPH and AM was the least uncoupled at ~1%, compared with 23% with Cys and 35% with NAC.

Determination of the oligomeric state

Size exclusion chromatography was used to determine that recombinant AsFMO exists in two oligomeric states, 151,000 ± 4000 Da and 57,000 ± 2000 Da, which correspond to trimeric and monomeric forms, respectively (the predicted mass based on the amino acid composition is 51,700 Da) (Fig. S6 and Table S1). These two forms were observed using different enzyme preparations, with 12 ± 2% being trimeric and the rest being monomeric. When the enzyme was incubated with Cys prior to separation based on size exclusion, the trimeric form was no longer observed. When the same experiment was repeated with $NADP^+$, no changes were noticed (data not shown).

Reductive half-reaction

The reaction of oxidized AsFMO with NAD(P)H was monitored using a stopped-flow spectrophotometer under anaerobic conditions. With NADPH in the absence of Cys, bleaching of the peak at 450 nm occurred in two phases. In addition, we observed that a stable broad band formed between 520 and 650 nm (Fig. 3), which correlated with the slow phase of reduction at 450 nm. The fast phase (k_{fast}) corresponded to 82% of the amplitude change. The rate constants of the slow phase (k_{slow}) and the formation of the broad band (k_{570}) were much lower than the k_{cat} with Cys (Table 2). The value for k_{fast} was constant even at 20 μM NADPH; thus, we estimate that the dissociation constant (K_d) for NADPH for this enzyme population is much lower (at least 10 times lower). The k_{slow} depended on the NADPH concentration, and a K_D of 15 μM was determined for this enzyme form. Formation of the long-wavelength band also exhibited dependence on the NADPH concentration, with a K_D of 33 μM. When AsFMO was incubated with Cys prior to mixing with NADPH, reduction occurred as a single phase and the formation of the long-wavelength band was observable only at low concentrations of NADPH. When AsFMO was reduced with NADH without Cys, the reaction was also biphasic, however, the formation of the long-wavelength band was not observed (Fig. S7). The values for both rate constants were lower than observed with NADPH. In addition, the K_D for NADH was much higher than that for NADPH (Table 2).

The stereospecificity of hydride transfer was probed using pro-*R*-[4-^{2}H]NADPH or pro-*S*-[4-^{2}H]NAPDH to reduce AsFMO when no substrate was present. From this experiment, it was observed that AsFMO exhibited kinetic isotope effects of 5.4 ± 0.1 with pro-*R*-[4-^{2}H]NADPH and 2.2 ± 0.05 with pro-*S*-[4-^{2}H]NADPH, demonstrating stereospecificity for pro-*R*-hydrogen. Formation of the long-wavelength band (k_{570}) and the second phase of reduction (k_{slow}) were not affected by isotopic substitution (Fig. S8 and Table S2).

Oxidative half-reaction

During the oxidative half-reaction, a peak rapidly formed at 370 nm, consistent with formation of the C4a-hydroperoxyflavin intermediate (Fig. 4). This peak was most prominent in the absence of substrate, decaying after ~7 s into the fully oxidized enzyme. The rate of C4a-hydroperoxyflavin intermediate formation (k_{OOH}) was enhanced in the presence of Cys. The rate of oxidation in the absence of Cys (k_{H2O2}), which reports on H_2O_2 elimination, was several orders of magnitude lower than k_{OOH}. In the presence of Cys, turnover occurs and the observed change in absorbance corresponds to substrate hydroxylation (k_{ox}) (Table 3). This process occurs in two phases, with the $k_{ox,slow}$ having a value similar to k_{cat} with Cys. Decay of the long-wavelength band from 520 to 650 nm was ~1–2 s^{-1}, with or without Cys.

Depending on the protein batch, the oxidation of AsFMO varied. Some preparations exhibited a two-phase oxidation without Cys, instead of a single-phase oxidation (Fig. S9). The fast phase of this experiment was 3.3 ± 0.3 s^{-1}, which was very similar to the $k_{ox,fast}$ observed during oxidation with Cys. Both rates are much higher than the k_{cat} value.

Structure determination

The structure of AsFMO complexed with FAD was determined at 2.08-Å resolution using selenomethionine (Se-Met) single-wavelength anomalous diffraction phasing (Fig. 5*A*). The structure exhibits the expected fold for an FMO, consisting of large and small, 3-layer $\beta\beta\alpha$ domains. The larger domain binds FAD, while the smaller one presumably binds NADPH. The FAD binds with its ADP moiety mainly interacting with the larger domain and the isoalloxazine located in the space between the two domains (Fig. 5*A*). The *si* face of the isoalloxazine is buried, while the *re* face is available for catalysis; this is expected for FMOs. Analysis of the protein-protein interfaces in the crystal lattice with PDBePISA (34) revealed no stable

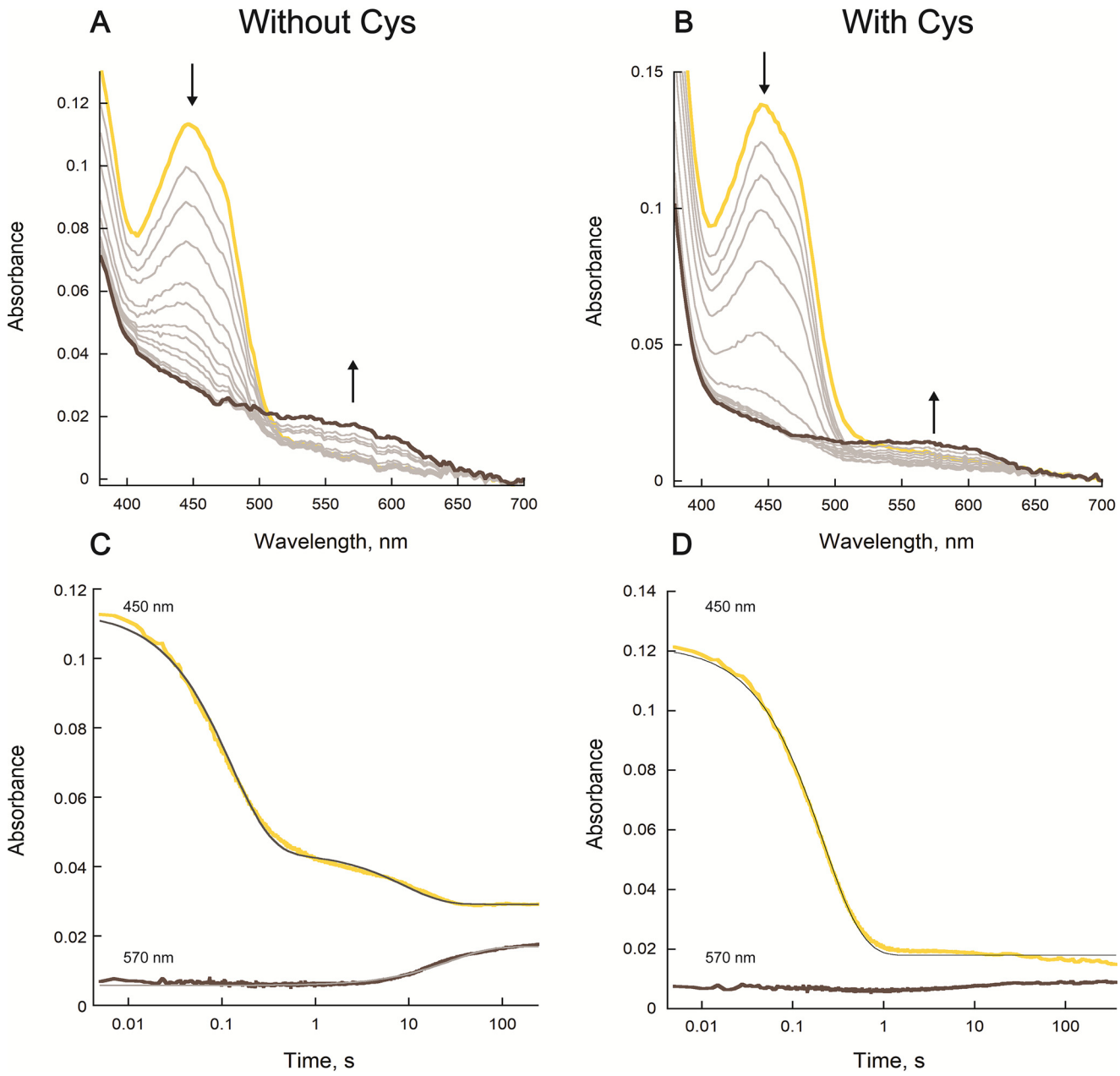

Figure 3. Changes in the flavin spectra during reduction with NADPH. Changes in the flavin spectra during reduction with NADPH were analyzed in the absence (*A*) or presence (*B*) of 100 mM Cys. The direction of change in absorbance is shown with *arrows*. The typical reduction at 450 nm is observed in addition to an increase in a long-wavelength band with an absorbance maximum at 570 nm. The initial spectrum is shown in *yellow* and the final spectrum in *brown*. In the absence of 100 mM Cys. (*C*), the absorbance changes at 450 nm best fit to Equation 4 and at 570 nm to Equation 5. In the presence of Cys (*D*), the absorbance at 450 nm best fit to Equation 3 and at 570 nm to Equation 5. Absorbance changes at 450 nm are shown in *yellow* and those at 570 nm in *brown*.

Table 2
Reductive half-reaction kinetic parameters for AsFMO in the absence or presence of 100 mM Cys

Rate constant	Cofactor[a]	Without Cys	With Cys
k_{fast} (s^{-1})	NADPH	7.6 ± 0.3	4.8 ± 0.1
k_{slow} (s^{-1})	NADPH	0.13 ± 0.003	N.A.[b]
k_{570} (s^{-1})	NADPH	0.050 ± 0.003	N.A.
$K_{D,fast,}$ (μM)	NADPH	<2	<2
$K_{D,slow}$ (μM)	NADPH	15 ± 2	N.A.
$K_{D,570}$ (μM)	NADPH	33 ± 2	N.A.
$k_{red,fast}$ (s^{-1})	NADH	4.3 ± 0.03	N.A.
$k_{red,fast}$ (s^{-1})	NADH	0.70 ± 0.10	N.A.
$K_{D,fast}$ (μM)	NADH	84 ± 4	N.A.
$K_{D,slow}$ (μM)	NADH	77 ± 5	N.A.

[a] Conditions were 50 mm HEPES pH 7.5.
[b] N.A., not applicable.

interfaces, suggesting that AsFMO may be predominantly monomeric in solution.

Query of the PDB with PDBeFold (35) revealed several FMOs as structural neighbors of AsFMO (36–40), the closest being pyrrolizidine alkaloid N-oxygenase from the grasshopper *Zonocerus variegatus* (ZvPNO) (PDB code 5NMW; 31% sequence identity to AsFMO) (38). AsFMO and ZvPNO superimpose with a root mean square deviation (RMSD) of 1.4 Å (Fig. 5*B*). The C terminus is a point of departure between the two structures; AsFMO has a 13-residue α-helix at the C terminus, whereas ZvPNO has a β-hairpin. The FADs of AsFMO and ZvPNO have slightly different ribityl conformations (Fig. 5*C*).

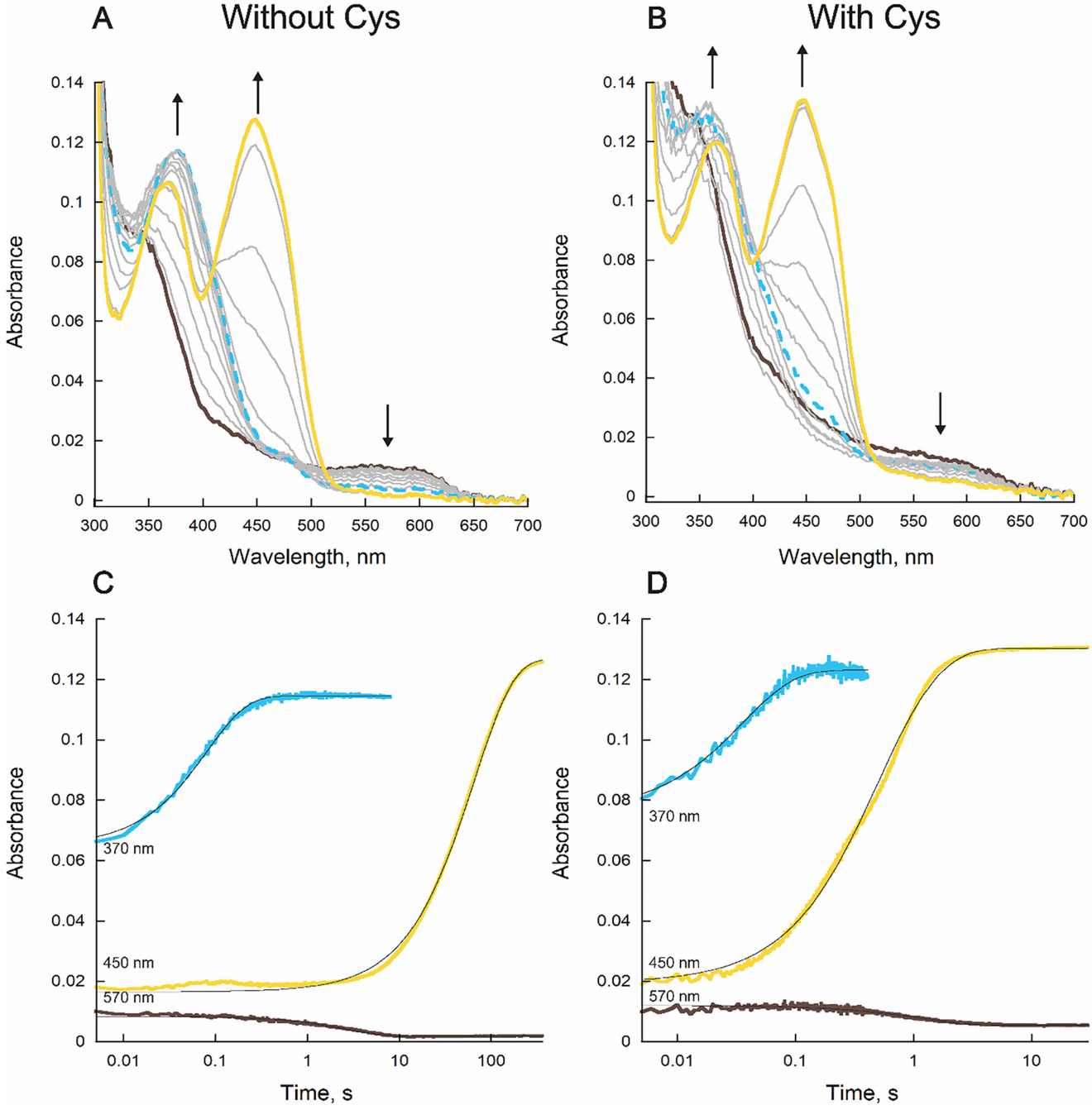

Figure 4. AsFMO oxidation. *A* and *B*, spectral changes of reduced AsFMO reacted with 300 μM O_2, monitored over 300 s, in the absence (*A*) or presence (*B*) of Cys (100 mM). The spectra of the reduced flavin is shown in *brown*, the C4a-hydroperoxyflavin intermediate in *blue*, and oxidized flavin in *yellow*. Direction of change in absorbance is shown with *arrows*. *C*, changes in the flavin absorbance at 370 nm (*blue*) (fit with Equation 5), 450 nm (*yellow*) (fit to Equation 5), and 570 nm (*brown*) (fit to Equation 3). *D*, same as in *C* but in the presence of 100 mM Cys.

Table 3

Oxidative half-reaction kinetic parameters for AsFMO in the absence or presence of 100 mM Cys

Rate constant	Cofactor[a]	Without Cys	With Cys
k_{OOH} (M^{-1} s^{-1})	NADPH	5500 ± 400	3400 ± 200
k_{H2O2} (s^{-1})	NADPH	0.002 ± 0.0005	N.A.[b]
$k_{ox,slow}$ (s^{-1})	NADPH	N.A.	1.20 ± 0.08
$k_{ox,fast}$ (s^{-1})	NADPH	N.A.	3.1 ± 0.01

[a] Conditions were 50 mm HEPES pH 7.5.
[b] N.A., not applicable.

In AsFMO, the 3′-OH is below the pyrimidine ring of the isoalloxazine and is hydrogen bonded to the FAD N1. In ZvPNO, the 3′-OH points toward Tyr307. The difference may be due to the replacement of Tyr307 with Pro342 in AsFMO. Steric clash with Pro342 would prevent the 3′-OH in AsFMO from adopting the conformation seen in ZvPNO. As a result, the two flavins differ by a crankshaft rotation involving the 2′-OH and 3′-OH. We note that the FAD conformation of AsFMO is very similar to that of FMO from *Schizosaccharomyces pombe* (PDB code 2GV8), which also has a Pro342 (40).

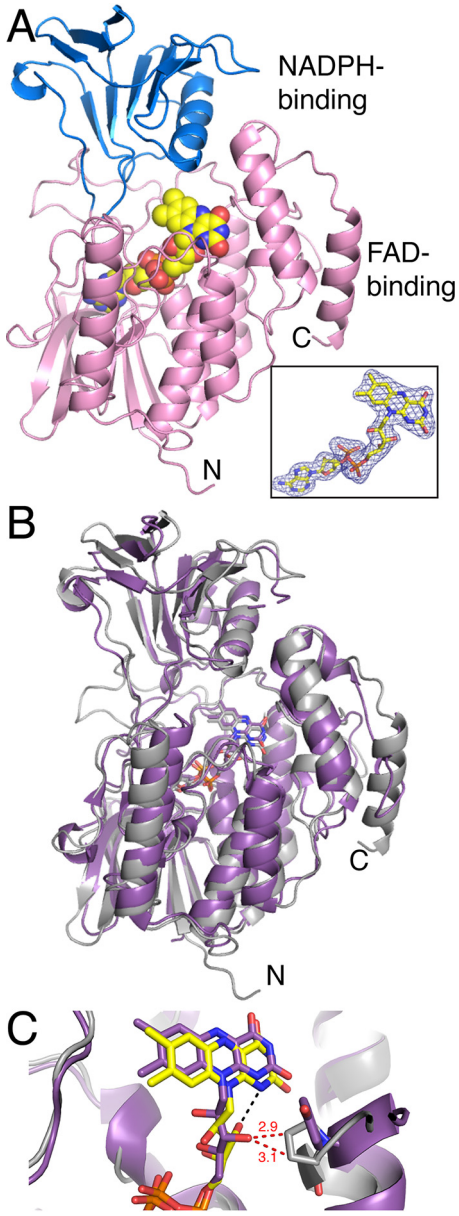

Figure 5. Structure of AsFMO. *A*, fold of AsFMO. The FAD- and NADPH-binding domains are colored *pink* and *blue*, respectively. FAD is shown as *yellow spheres*. *Inset*, FAD covered by a polder omit map (4σ). *B*, superposition of AsFMO (*gray*) and ZvPNO (PDB code 5NMW) (*purple*). *C*, comparison of the FAD conformations of AsFMO (*gray*) and ZvPNO (PDB code 5NMW) (*purple*). *Black dashes* indicate an intra-FAD hydrogen bond in AsFMO. *Red dashes* denote predicted clashes between the FAD of pyrrolizidine alkaloid N-oxygenase and Pro342 in AsFMO.

Discussion

AsFMO has been reported to perform a chiral oxidation of SAC, forming alliin, the stable precursor of allicin (15). This proposed function has been generally accepted in the literature, with a prior publication reporting that recombinant AsFMO in yeast extracts exhibits activity with SAC, albeit at a low rate (V_{max} = 3.4 ± 1.2 pmol μg^{-1} h^{-1}) (14, 15, 22, 41, 42). One of the aims of this study was to characterize the proposed enzymatic activity and to further validate the role of AsFMO in allicin biosynthesis. However, despite extensive attempts, we were unable to demonstrate activity of AsFMO with SAC. This lack

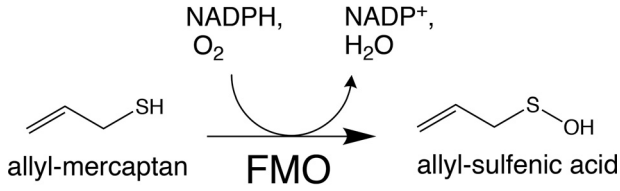

Scheme 2. Proposed function of AsFMO in allicin biosynthesis.

of activity was not due to isolation of an inactive enzyme, since we tested several other potential substrates and showed that the enzyme was active with Cys, NAC, and AM. Furthermore, with AM, AsFMO was highly coupled. Analysis of the catalytic efficiencies (k_{cat}/K_m) and coupling suggest that AM and NADPH are the preferred substrates (Table 1). Clearly, our data do not support the proposed activity of AsFMO with SAC but instead suggest that AsFMO contributes directly to the biosynthesis of organosulfur compounds by oxidizing AM into allyl sulfenic acid (Scheme 2). This physiological role is supported by the fact that AM is a significant garlic metabolite, making up 1.4% of the volatile compounds in garlic (43, 44). In addition, AsFMO would be regulated by the restrictive oxygen conditions inside the garlic cytosol, which fits with the current assumption that plant tissue damage is essential for allicin production, as AsFMO would be active when exposed to atmospheric oxygen (12, 45).

The observed activity with Cys and NAC could also be of physiological relevance, as Cys has been shown to be important for biosynthesis of organosulfur compounds in garlic (46–48). NAC has also been reported to be abundant in water-soluble extracts of garlic samples, and it is thought to be involved in the biosynthesis of *N*-acetyl-*S*-allyl-L-cysteine (49, 50). The activity of AsFMO with Cys could account for production of L-cystine in garlic (0.65 mg/g according to the USDA; FoodData Central code 169230). The specific role of cystine in garlic or other *Allium* plants is unknown; however, it has been shown that alliinase from *A. sativum* exhibits cystine lyase activity, which, in the presence of potassium polysulfide, can lead to the formation of organosulfur compounds like diallyl disulfide and diallyl trisulfide (51).

Stopped-flow kinetic analysis allowed for detailed characterization of the catalytic cycle of AsFMO (Scheme 3). The reductive half-reaction starts with the oxidized enzyme binding NADPH with high affinity (Scheme 3, *A* and *B*). Flavin reduction occurs in two phases, with pro-*R* stereospecificity (Scheme 3*C*). The fast phase is much faster than k_{cat}, indicating that it is not the rate-limiting step of the reaction. We suggest that the slow phase, which provides only 18% of the amplitude change, represents the reaction of an enzyme population that is present in a different conformation (see below). Substrate binding can occur before or after NADPH binding and only slightly decreases the rate constant for flavin reduction. This effect has been observed in other class B FMOs and is thought to be caused by conformational changes induced by substrate binding (31). The oxidative half-reaction starts with reaction of oxygen with the reduced enzyme in complex with $NADP^+$ (Scheme 3*D*). The C4a-hydroperoxyflavin can be observed with a characteristic peak at 370 nm (Fig. 4*A*). In the absence of

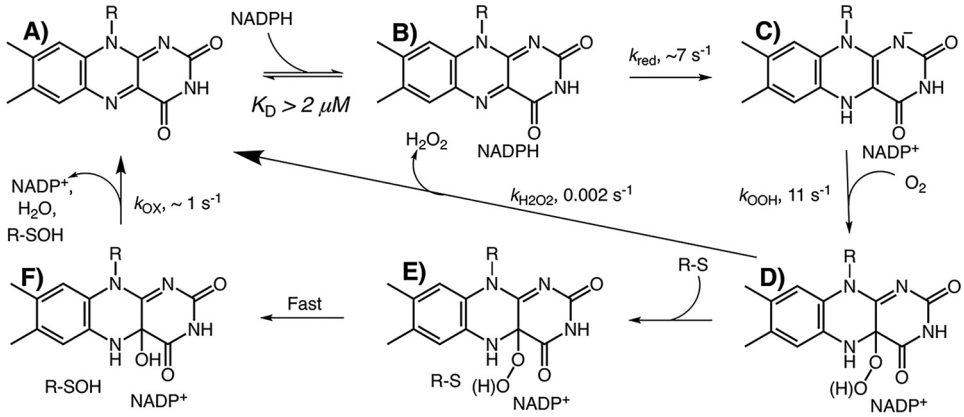

Scheme 3. Proposed mechanism of AsFMO. Each reaction cycle begins with an oxidized enzyme (*A*). NADPH binds tightly to AsFMO (*B*) and transfers the pro-*R*-C4-hydride of the nicotinamide to the N5 of FAD, producing a flavin hydroquinone (*C*). The reduced flavin then transfers an electron to oxygen, temporarily producing a flavin semiquinone and superoxide before forming a C4a-hydroperoxyflavin intermediate stabilized by $NADP^+$ (*D*). The substrate (R-S) enters the active site (*E*) and reacts with the distal -OH group of the C4a-hydroperoxyflavin intermediate through nucleophilic attack, producing the hydroxylated product (R-SOH) and a C4a-hydroxyflavin (*F*). The final step is dehydration of the C4a-hydroxyflavin to regenerate the oxidized flavin and to release the products.

hydroxylatable substrate, this intermediate is stable, and the enzyme oxidizes by the slow release of H_2O_2 (~300 times slower than k_{cat}) (Scheme 3*D*). This is due to stabilization by $NADP^+$, which is essential to ensure coupling of the reductive and oxidative half-reactions. In the presence of hydroxylatable substrate, formation of the C4a-hydroperoxyflavin is slightly enhanced. Here, hydroxylation and flavin oxidation take place by release of H_2O and other products (Scheme 3, *E* and *F*). This process occurs in two phases and the $k_{ox,slow}$ and k_{cat} values are very similar, suggesting that flavin oxidation is at least partially rate-limiting (Table 3). We noticed that the amplitude of the $k_{ox,fast}$ does not indicate the prominent phase (~30%) and varies between experiments. It is possible that this observed fast phase is related to a population of enzyme that does not stabilize the C4a-hydroperoxyflavin intermediate. Interestingly, the amplitude of the fast phase is similar to the percentage of uncoupling observed at saturating conditions of Cys and NADPH (23%) (Fig. 2). This suggests that the population of enzyme contributing to the fast phase of oxidation could be responsible for the uncoupled reaction.

The kinetic characterization is consistent with AsFMO being a member the class B flavin-dependent monooxygenase mechanism (52). Members of this class share specificity for NADPH, pro-*R* stereoselectivity, and stabilization of the C4a-hydroperoxyflavin, as demonstrated for AsFMO (29, 53–55).

A unique aspect observed with AsFMO was the formation of a broad band between 520 and 650 nm when reduced by NADPH. This band is very stable, decaying only when the reduced enzyme is exposed to molecular oxygen. It is possible that this band represents the formation of a charge-transfer complex. This assumption is reasonable, as charge-transfer complexes have been reported for other FMOs, including the plant enzyme YUCCA monooxygenase (24). The fact that AsFMO reduction at 450 nm is completed in two phases, with the slow phase correlating to the formation of the long-wavelength band, suggests that there are two populations of AsFMO that interact differently with $NADP^+$. The slow phase at 450 nm is not isotope sensitive, suggesting either that the change in absorbance is related to conformational changes or that, with this enzyme population, hydride transfer is not rate-limiting. The possibility of different enzyme forms is supported by the size exclusion chromatography results showing the presence of a trimeric form that is absent in the presence of Cys. The low rate associated with the long-wavelength band formation (0.03 s^{-1}), especially when compared with the k_{cat} under similar conditions (1.2 s^{-1}), demonstrates that it is likely not catalytically relevant. It is possible that this enzyme population is the one reacting faster with oxygen ($k_{ox,fast}$), leading to uncoupling.

The structure of AsFMO complexed with FAD was determined at 2.08 Å. This structure contains a two-domain architecture for binding of FAD and NADPH, which is common in class B flavin monooxygenases. The active site shows that the *re* face of the isoalloxazine ring is exposed for catalysis. There are structural homologs of AsFMO from *Zonocerus variegatus,* which is proposed to be a pyrrolizidine alkaloid N-oxygenase. There are some differences in the interaction with the flavin cofactor, which are also observed in the FMO from *S. pombe*.

The structure provides insight into the preference for AM over SAC as the substrate. A reasonable model of AsFMO complexed with $NADP^+$ was built by superimposing the structure of *S. pombe* FMO complexed with NADPH (PDB code 2GV8) onto the AsFMO structure. Inspection of the model revealed a tunnel that provides access to C4a of the FAD, which we propose to be the substate-binding tunnel. Steric constraints suggest that the substrate must be threaded through a narrow entranceway (Fig. 6*A*). A model of SAC in the tunnel suggests there may not be sufficient room to accommodate the three terminal C atoms of SAC while bringing the S atom close to C4a (Fig. 6*B*). No such impediment is observed with AM (Fig. 6*C*).

In conclusion, this paper describes the activity and kinetic mechanism of AsFMO. Unexpectedly, AsFMO does not exhibit significant activity with SAC, the generally accepted *in vivo* substrate. Instead it is active with Cys, NAC, and AM, with a distinct preference for AM. Thus, our data do not support the generally accepted role of AsFMO in allicin biosynthesis (Scheme 1). We propose that AsFMO catalyzes a feeder pathway for allicin biosynthesis by catalyzing the oxidation of AM to allyl sulfenic acid (Scheme 2). Presumably, a currently

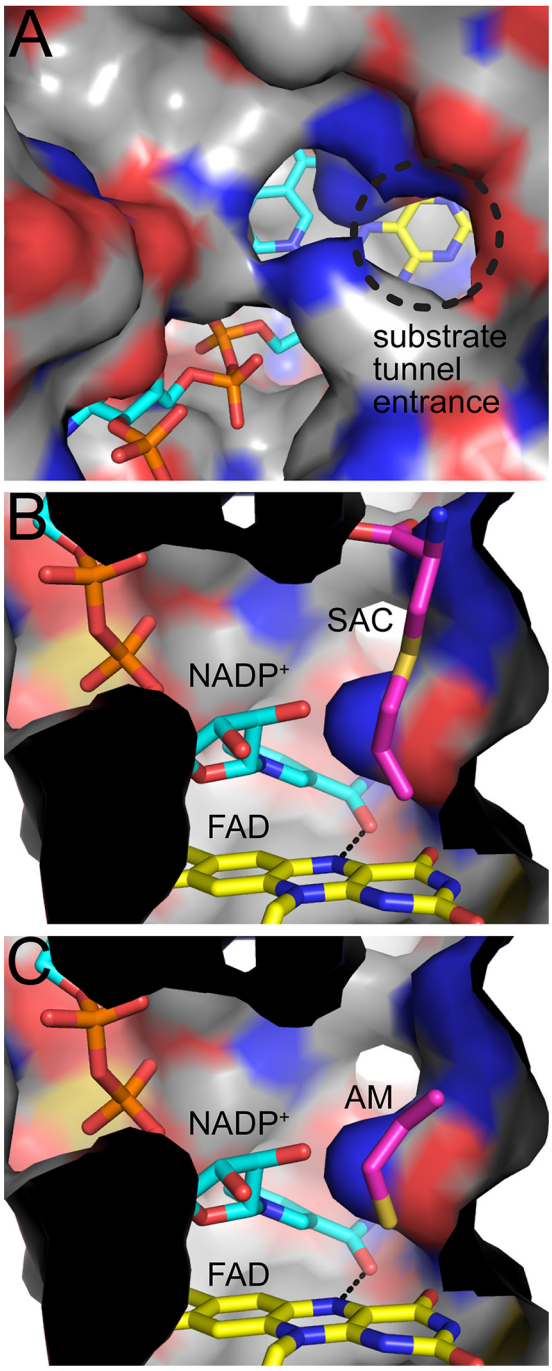

Figure 6. Models of SAC and AM in the active site of AsFMO. *A*, view into the proposed substrate tunnel. $NADP^+$ was modeled based on the structure of FMO from *S. pombe* (PDB code 2GV8). FAD and $NADP^+$ are colored *yellow* and *cyan*, respectively. *B*, cutaway view of a model of SAC in the substrate tunnel. *C*, cutaway view of a model of AM in the substrate tunnel.

undiscovered enzyme catalyzes the oxidation of SAC to allicin. The crystal structure and biochemical characterization represent the first for a specific FMO from plants.

Experimental Procedures

Materials

The gene coding for AsFMO (accession number AB924383) was synthesized and codon-optimized by GenScript (Piscataway, NJ). It was subcloned into pET15b for expression with an N-terminal His_6 tag in *Escherichia coli*. Primers for subcloning and sequencing were purchased from Integrated DNA Technologies (Newark, NJ). Oneshot BL21 (DE3) and Top10 *E. coli* cells were purchased from Thermo Fisher Scientific (Waltham, MA) and used for protein expression and DNA amplification, respectively. Reagents for AsFMO crystallization were from Hampton Research (Aliso Viejo, CA). All gases were purchased from Airgas (Radnor, PA). Stereospecifically deuterated NADPH (pro-*R*-[4-^{2}H]NADPH and pro-*S*-[4-^{2}H]NAPDH) was synthesized following published procedures (56).

Gene subcloning and protein expression

The pET15b vector expressed a protein that was largely insoluble. To overcome this problem, the AsFMO gene was inserted into the pVP56K vector in-frame for expression with an N-terminal His_8-MBP, as described previously (30, 57, 58). Protein expression was performed in BL21(DE3) cells using an autoinduction method, as described previously (58). Cells were harvested by centrifugation at 5000 × *g* and stored at −70 °C.

For expression of Se-Met-labelled AsFMO, a minimal medium kit, purchased from Medicillin (Chicago, IL), was used. Cells were grown in Luria-Bertani broth for 8 h at 37 °C, with agitation at 250 rpm; 50 ml of minimal medium was inoculated with 1 ml of the Luria-Bertani broth culture and grown overnight at 37 °C, with agitation at 250 rpm. Protein expression was performed in 1 liter of minimal medium inoculated with 10 ml of the overnight culture. The culture was grown at 37 °C with constant agitation (250 rpm) until an A_{600} of 0.6 was reached. To inhibit methionine production, 0.15 g of leucine, isoleucine, and valine and 0.3 g of lysine, threonine, and phenylalanine were added, along with 0.15 g of Se-Met, into each 1-liter culture. After incubation of the culture with the amino acids for 15 min, protein expression was induced with 0.1 mM isopropyl β-D-thiogalactopyranoside. The cultures were grown overnight at 18 °C, and the cells harvested by centrifugation and stored at −70 °C.

Protein purification

Cell paste was resuspended in 150 ml Buffer A (25 mM HEPES, pH 7.5, 300 mM NaCl, 25 mM imidazole, and 10% glycerol), supplemented with 1 mg/ml lysozyme, 1 mg/ml DNase, 1 mg/ml RNase, 1 mM phenylmethylsulfonyl fluoride, and 150 μM FAD, and incubated for 30 min with constant stirring. The cells were lysed by sonication at 70% amplitude with cycles of 5 s on and 10 s off for 5 min. Insoluble material was removed by centrifugation at 30,000 × *g* for 1 h at 4 °C. The supernatant was loaded onto three in-tandem 5-ml nickel ion-charged IMAC columns equilibrated in Buffer A, using an AKTA Prime system (GE Healthcare, Chicago, IL). After protein loading was complete, the columns were washed with ~40 ml of Buffer A and ~ 20 ml of Buffer A containing 30 mM imidazole. AsFMO was eluted with Buffer B (25 mM HEPES, pH 7.5, 300 mM NaCl, 300 mM imidazole, and 10% glycerol). Fractions that contained the MBP-AsFMO fusion protein, as observed by their yellow color, were pooled before the addition of His_6-TEV protease (1 part TEV protease per 30 parts MBP-AsFMO). The reaction

(~20 ml) was dialyzed overnight at 4 °C in 2 liters of 25 mM HEPES, pH 7.5, with 100 mM NaCl.

The cleaved AsFMO product was separated from the His_8-MBP protein and His_6-TEV protease by loading the protein mixture onto two 5-ml IMAC columns that had been equilibrated with Buffer C (25 mM HEPES, pH 7.5, and 100 mM NaCl). AsFMO was collected in the flow-through fraction, and MBP and TEV protease were eluted with 100% Buffer D (25 mM HEPES, pH 7.5, 100 mM NaCl, and 300 mM imidazole). The flow-through fractions were yellow, and SDS-PAGE analysis showed a single band corresponding to AsFMO (Fig. S1). These fractions were pooled, concentrated using a 30-kDa centrifuge filter (Sigma Aldrich), and stored at −70 °C in Buffer C. The same method was used to purify Se-Met-AsFMO, with the addition of 1 mM tris(2-carboxyethyl)phosphine to all purification and storage buffers to prevent Se-Met oxidation.

NADPH oxidation assay

NADPH oxidation assays were performed in triplicate in 50 mM HEPES pH 7.5 at 20 °C using an Agilent 8453 spectrophotometer. Assay mixtures containing various concentrations of Cys (0–150 mM) and 0.1 mM NADPH were prepared in a volume of 200 μl. To initiate the reaction, 1 μM AsFMO was added immediately before measurements were taken. The change in absorbance at 340 nm was monitored for 2 min.

Oxygen consumption assay

The activity of AsFMO was measured using an oxygen electrode system (Hansatech, Amesbury, MA). All assays were performed in 1 ml of 50 mM HEPES, pH 7.5, and initiated by the addition of 1–2 μM enzyme. The steady-state kinetics of AsFMO were determined by varying the concentration of substrate or NAD(P)H (0.01–1.0 mM) with saturated concentrations of Cys (150 mM) at the oxygen air saturation level. The data were fitted to the Michaelis-Menten (Equation 1).

$$\frac{v_i}{[E]} = \frac{k_{cat}[S]}{K_m + [S]} \quad \text{(Eq. 1)}$$

$[E]$ represents the AsFMO concentration, $[S]$ is the concentration of substrate, k_{cat} is the turnover number of the reaction, and K_m is the Michaelis constant.

For data that exhibited substrate inhibition, such as NADPH saturation (Fig. 1*B*), the data were analyzed with Equation 2. Here, K_i is the substrate inhibition constant.

$$\frac{v_i}{[E]} = \frac{k_{cat}[S]}{K_m + [S] + \frac{[S]^2}{K_i}} \quad \text{(Eq. 2)}$$

The rate constant of hydrogen peroxide production by AsFMO was measured by determining the effect of catalase on the rate of oxygen consumption. It was determined that 1 mg/ml catalase (Sigma Aldrich) did not decrease or inhibit the activity of AsFMO, by verifying that NADPH oxidation did not change in the presence of catalase (Fig. S5). In an assay containing 1 mg/ml catalase, the rate of oxygen consumption by AsFMO was measured in the presence of 150 mM Cys, 25 mM AM, or 150 mM NAC and 0.25 mM NADPH or 0.5 mM NADH, and results were compared with those of assays without catalase. The difference between the initial rates was used to calculate the rate of hydrogen peroxide production, taking into account the stoichiometry of the catalase reaction (2 mol H_2O_2 consumed to 1 mol O_2 produced).

Substrate consumption assay

To measure the consumption of the amino acid substrates Cys and SAC, fluorenylmethyloxycarbonyl chloride and 1-adamantylamine derivatization was used (59). Assays were performed at 200 μl with 15 mM substrate, 5 mM NADPH, and 5 μM AsFMO in 50 mM HEPES pH 7.5. At different time points between 0.5 and 5 h, 30 μl of the reaction mixture was quenched with 150 μl acetonitrile, and the precipitant removed by centrifugation at 14,000 rpm for 2 min. An aliquot of 130 μl of the quenched reaction mixture was then transferred to a conical 96-well plate, and 25 μl of 0.2 M borate pH 8.5 was added. To this solution, 3.25 μl of 50 mM L-ornithine was added as a standard. To initiate derivatization, 10 μl of 158 mM fluorenylmethyloxycarbonyl chloride prepared in acetonitrile was added. The plate was shaken at room temperature for 5 min before the reaction was quenched with 150 μl of 40 mM 1-adamantylamine prepared in 50% acetonitrile. The assay mixture was shaken (100 rpm) for 15 min and centrifuged before 2 μl of the sample was injected for separation, using an ACCQ-TAG ULTRA C_{18} column attached to a Waters Acquity UPLC system (Milford, MA) equipped with a UV-visible detector. Samples were monitored at 263 nm. Buffers A and B were 0.1% TFA in water and 0.1% TFA in acetonitrile, respectively. Samples were eluted with a gradient of 20–85% Buffer B for 13 min. The $area_{substrate}/area_{l\text{-}ornithine}$ was calculated using the integrated area under the curve for each sample. Using this analysis, a standard curve with 1–20 mM substrate was constructed and used to measure the change in concentration.

Product determination with Cys as substrate

The AsFMO storage buffer (25 mM HEPES, 100 mM NaCl, pH 7.5) was changed using a 10-ml gel filtration column equilibrated in 10 mM ammonium bicarbonate pH 7.5. All other reagents were prepared in 10 mM ammonium bicarbonate and the pH was adjusted to 7.5, as required. The reaction mixture consisted of 20 mM Cys and 2.5 mM NADPH. The reaction was initiated by addition of 5 μM AsFMO and then incubated for 2 h before removal of the enzyme by passing the solution through a 10-kDa centrifugal filter. The reaction mixture was acidified by adding 1 part 6 N HCl to 100 parts assay to prevent any unwanted cysteine oxidation. Samples were stored at −70 °C until submission to the Virginia Tech MS incubator (Blacksburg, VA). All electrospray ionization mass spectra were collected by direct injection for accurate mass analysis on an Agilent 6220 TOF LC–MS.

Detection of sulfenic acid

Assays were completed with 50 mM 5,5-dimethyl-1,3-cyclohexanedione (dimedone) (60) or *cis*-5-norbornene-endo-2,3-dicarboxylic acid (norbornene) (61) with 25 μM AsFMO, 2 mM

NADPH, and 5 mM Cys. The reaction was incubated for 2 h, at which point AsFMO was removed with a 10-kDa centrifugal filter. This assay was performed in 50 mM HEPES at pH 7.5 and ammonium acetate at pH 5.5.

The reaction mixture was injected at 10 μl onto a Shimadzu HPLC system (Columbia, MD) equipped with a Luna 5-μm C_{18} column (Phenomenex, Golden, CO). Samples were eluted with a gradient of water with 0.1% TFA to 30% acetonitrile with 0.1% TFA over 20 minutes, followed by a gradient to 100% acetonitrile with 0.1% TFA over 2 minutes and held for 5 minutes. Dimedone and any derivatives were detected at 260 nm, and norbornene and norbornene derivatives were detected at 260 nm.

Size exclusion chromatography

An AKTA Prime Plus FPLC system equipped with a HiPrep 16/60 Sephacryl S-200 HR column (GE Healthcare) was used to determine the oligomeric state of AsFMO. The column was equilibrated with 50 mM potassium phosphate pH 7.5 and 100 mM NaCl at a flow rate of 1 ml/min. A standard curve was constructed using a high-molecular weight marker kit (GE Healthcare) supplemented with RNase (Sigma Aldrich, St. Louis, MO) and TEV protease. The curve consisted of ferritin (440 kDa), aldolase (160 kDa), conalbumin (75 kDa), ovalbumin (43 kDa), His_6-TEV protease (27 kDa), and RNase (13 kDa). A 500-μl sample of AsFMO (3 mg/ml) was filtered with a 0.22-μm cellulose acetate filter and injected onto the column. For the substrate sample, AsFMO was incubated with 150 mM Cys for 15 min prior to injection. AsFMO-containing fractions were verified by 12% acrylamide SDS-PAGE.

Stopped-flow spectrophotometry

All stopped-flow assays were performed with a SX20 stopped-flow spectrophotometer equipped with a photodiode array detector (Applied Photophysics, Surrey, UK) housed inside an anaerobic chamber (COY Laboratories, Grass Lake, MI). A detailed protocol of the experimentation was described previously (62). In brief, the sample-handling unit was scrubbed of potential oxygen contamination overnight using anaerobic buffer solution containing glucose oxidase and dextrose. The protein sample and 1 M Cys stock were deoxygenated with 20 cycles of high vacuum (20 s) and ultrapure argon (10 s). The reducing cofactors were dissolved in anaerobic buffer. All assays were performed in 50 mM HEPES pH 7.5.

For the reductive half-reaction, 20 μM AsFMO was mixed with 20–800 μM NADPH, and spectral changes from 190 to 850 nm were recorded in a logarithmic scale for 240 s (no Cys) or 360 s (Cys). AsFMO reduction with Cys was performed by incubating the enzyme with 200 mM Cys prior to sample mixing. AsFMO reduction with NADH was performed by mixing 20 μM AsFMO with 100–1400 μM NADH, with spectral changes measured for 180 s. The changes at 450 nm during reduction were best fit with a single-exponential (Equation 3) or double-exponential (Equation 4) decay equation.

$$Abs = Ae^{-k_{obs}t} + C \qquad \text{(Eq. 3)}$$

$$Abs = A_1e^{-k_{obs,1}t} + A_2e^{-k_{obs,2}t} + C \qquad \text{(Eq. 4)}$$

For single-exponential decay, A is the amplitude, k_{obs} is the observed rate, and C is the final absorbance. For double-exponential decay, the same terms apply with the modification that A_1 is the amplitude of change that occurs during the first phase, A_2 is the amplitude change that occurs during the second phase, $k_{obs,1}$ is the observed rate of the first phase, and $k_{obs,2}$ is the observed rate of the second phase. AsFMO reduction with NADPH at 450 nm was best fit with Equation 4, while reduction with NADH or in the presence of Cys was best fit with Equation 3. Changes at 570 nm during reduction were analyzed using a single-exponential rise equation (Equation 5).

For the oxidative half-reaction, a reduced enzyme stock of 20 μM AsFMO mixed with 20 μM NADPH was prepared. An oxygen-saturated buffer was prepared by following a procedure described previously (62). The reduced enzyme solution was mixed with 400–1100 μM oxygen, with measurement being recorded for 300 s (no Cys) or 30 s (Cys). Changes at 370 nm and 450 nm were analyzed using a single-exponential (Equation 5) or double-exponential (Equation 6) rise equation. All similar variables represent the same as described for Equation 3 and Equation 4. Variable D represents the initial absorbance at the wavelength.

$$Abs = A_1(1 - e^{-k_{obs}t}) + D \qquad \text{(Eq. 5)}$$

$$Abs = A_1(1 - e^{-k_{obs,1}t}) + A_2(1 - e^{-k_{obs,2}t}) + D \qquad \text{(Eq. 6)}$$

The changes at 370 nm were best fit with Equation 5, while changes at 450 nm were best fit with Equation 6. The absorbance at 570 nm exhibited single-exponential decay and was analyzed with Equation 3.

The concentration dependence of the k_{obs} values for flavin reduction was analyzed with Equation 7, where k_{obs} is the observed rate, k_{red} is the rate constant for flavin reduction at saturating substrate concentration, and K_D is the dissociation constant for substrate binding.

$$k_{obs} = \frac{k_{red}[S]}{K_D + [S]} \qquad \text{(Eq. 7)}$$

In order to determine the bimolecular rate constant of C4a-hydroperoxyflavin formation (k_{OOH}), the data were fit to a linear equation. For the experiments that showed minimal rate changes at various concentrations of molecular oxygen (k_{H2O2} and k_{ox}), the average of these values was reported.

The kinetic isotope effect on the reductive half-reaction was determined using isotopically labeled pro(R/S)-[4-^{2}H]NADPH. The concentration was kept at 125 μM for the nondeuterated and deuterated cofactors. The kinetic isotope effect was calculated from the ratio of the k_{obs} value at 450 for the unlabeled cofactor to that for the labeled cofactor.

Crystallization

Crystal conditions for AsFMO were found by screening the conditions in crystal kits 1 and 2 from Hampton Research

Table 4
X-Ray diffraction and data collection statistics

	Phasing	Refinement
Space group	$P3_121$	$P3_121$
Unit cell parameters		
a and *b* (Å)	135.49	139.72
c (°)	86.44	77.87
Moles (ASU)	1	1
Wavelength (Å)	0.97910	0.97910
Resolution (Å)[a]	117.3–2.73 (2.86–2.73)	121.0–2.08 (2.14–2.08)
No. of observations[a]	492,880 (62,335)	583,633 (38,452)
No. of unique reflections[a]	24,584 (3179)	52,404 (3905)
$R_{merge}(I)$[a]	0.159 (2.940)	0.126 (1.673)
$R_{meas}(I)$[a]	0.163 (3.018)	0.132 (1.765)
$R_{pim}(I)$[a]	0.036 (0.670)	0.039 (0.555)
Mean I/σ[a]	20.8 (1.6)	15.6 (1.6)
$CC_{1/2}$[a]	0.999 (0.826)	0.999 (0.642)
Completeness (%)[a]	99.7 (98.0)	99.7 (96.7)
Multiplicity[a]	20.0 (19.6)	11.1 (4.8)
Anomalous completeness[a]	99.4 (95.9)	99.6 (94.9)
Anomalous multiplicity[a]	10.5 (10.3)	5.5 (4.8)
Δ_{anom} corr. between half-sets	0.304	−0.016
No. of protein residues		439
No. of atoms		
Protein		3,483
FAD		53
Water		157
R_{cryst}[a]		0.1782
R_{free}[a,b]		0.2037
RMSD		
Bonds (Å)		0.007
Angles (°)		0.896
Ramachandran plot[c]		
Favored (%)		97.48
Outliers (%)		0.00
Clash score (PR)[c]		1.3 (100)
MolProbity score (PR)[c]		1.15 (100)
Average *B* (Å^2)		
Protein		47.4
FAD		35.9
Water		47.3
Coor. error (Å)[d]		0.25
PDB code		6WPU

[a] Values for the outer resolution shell of data are given in parenthesis.
[b] 5% test set.
[c] From MolProbity. The percentile ranks (PR) for Clashscore and MolProbity score are given in parentheses.
[d] Maximum likelihood-based coordinate error estimate from PHENIX.

(Aliso Viejo, CA). Crystals were observed within 4 weeks in 1.6 M ammonium sulfate, 0.1 M NaCl, and 0.1 M HEPES, pH 7.5, when AsFMO (4.5 mg/ml) was incubated with 5 mM Cys. Large rod-shaped crystals with a trigonal point were obtained in 1.9 M ammonium sulfate, 0.1 M NaCl, and 0.1 M HEPES with microseeding. Droplets were prepared with an AsFMO/mother liquor/microseed ratio of 1:1.5:0.5. All trays were stored at 15 °C after preparation. The same conditions were used to obtain Se-Met crystals, with 1 mM tris(2-carboxyethyl)phosphine being present in any enzyme buffer used to prepare the sample. Crystals were grown for ~30 days. Crystals were incubated in a solution containing 25% glycerol, 1.8 M ammonium sulfate, 0.1 M HEPES, pH 7.5, and 2.5 mM NaCl for 2 min before they were flash-frozen in liquid nitrogen.

X-ray diffraction data collection, phasing, and refinement

X-ray diffraction data were collected in shutterless mode at NECAT beamline 24-ID-C at the Advanced Photon Source. The data set used for Se-Met single-wavelength anomalous diffraction phasing consisted of 1800 images covering 360° of rotation. The data set used for refinement consisted of 1000 images covering 200° of rotation. All data sets were integrated and scaled using XDS (63). Intensities were converted to amplitudes using Aimless (64). The space group is $P3_121$, with unit cell dimensions of $a = b = 139.7$ Å and $c = 77.9$ Å. The asymmetric unit contains one chain of AsFMO. The estimated solvent content is 71%, with a V_M of 4.25 Å^3/Da (65). Data processing statistics are listed in Table 4.

The initial phases were determined by Se-Met single-wavelength anomalous diffraction phasing using SHELXD (66) to identify Se sites, and the structure determination tools of PHENIX were used to perform density modification and automated building (67). The calculations identified a constellation of 12 Se sites of the 14 expected for one protein chain in the asymmetric unit. Density modification with automated model building in PHENIX produced a model consisting of 343 residues with $R_{work} = 0.42$ and $R_{free} = 0.45$. The model exhibited both α-helices and β-sheets, and these secondary structural elements were arranged in two 3-layer $\beta\beta\alpha$ domains, as expected for an FMO.

The model from autobuilding was the starting point for several rounds of manual building in Coot (68) and refinement against a 2.08-Å data set in PHENIX (69). Structure validation was performed using MolProbity and the wwPDB validation service (70, 71). Polder maps were used to validate the conformation of the FAD (72). Refinement statistics can be found in Table 4.

Data availability

The coordinates and structure factors have been deposited in the PDB under accession code 6WPU. We declare that all other data supporting the findings of this study are available within the article and its supporting information.

Acknowledgments—This work is based on research conducted at the Northeastern Collaborative Access Team beamlines, which are funded by the National Institute of General Medical Sciences from the National Institutes of Health (Grant P30 GM124165). This research used resources of the Advanced Photon Source, a U.S. Department of Energy (DOE) Office of Science User Facility operated for the DOE Office of Science by Argonne National Laboratory under Contract DE-AC02-06CH11357.

Author contributions—H. V. and P. S. conceptualization; H. V., A. C. C., J. P. S., N. S., H. G. N., and J. J. T. data curation; H. V., A. C. C., and P. S. formal analysis; H. V. and P. S. writing-original draft; H. V., J. J. T., and P. S. writing-review and editing; S. L. investigation; J. J. T. and P. S. resources; J. J. T. and P. S. visualization; J. J. T. and P. S. methodology; P. S. funding acquisition; P. S. project administration.

Funding and additional information—Research reported in this publication was supported by National Science Foundation Grants CHE 2003658 (to P. S.) and CHE-2003986 (to J. J. T.). H. V. was supported by the Virginia Tech Institute of Critical Technology and Applied Science Doctoral Scholars Fellowship. A. C. C. was funded in part by a Fulbright Science and Innovation Graduate Award.

Conflict of interest—The authors declare that they have no conflicts of interest with the contents of this article.

Abbreviations—The abbreviations used are: FMO, flavin-containing monooxygenase; AsFMO, *Allium sativum* flavin-containing monooxygenase; SAC, *S*-allyl-l-cysteine; Cys, l-cysteine; NAC, *N*-acetyl-l-cysteine; IMAC, immobilized metal affinity chromatography; AM, allyl mercaptan; TEV, tobacco etch virus; Se-Met, selenomethionine; MBP, maltose-binding protein; RMSD, root mean square deviation; ZvPNO, *Zonocerus variegatus* pyrrolizidine alkaloid N-oxygenase.

References

1. Petrovska, B. B., and Cekovska, S. (2010) Extracts from the history and medical properties of garlic. *Pharmacogn. Rev.* **4,** 106–110 CrossRef Medline
2. Hann, G. (1996) *History, folk medicine, and legendary uses of garlic in Garlic: The Science and Therapeutic Application of Allium sativum L. and Related Species*, pp. 37–107, Williams and Wilkins, Baltimore, MD
3. Harris, J., Cottrell, S., Plummer, S., and Lloyd, D. (2001) Antimicrobial properties of *Allium sativum*. *App. Microbiol. Biotechnol.* **57,** 282–286 CrossRef Medline
4. Shang, A., Cao, S., Xu, X., Gan, R., Tang, G., Cork, H., Mavumangwana, V., and Li, H. (2019) Bioactive compounds and biological functions of garlic (*Allium sativum L.*). *Foods* **8,** E246 CrossRef
5. Borlinghaus, J., Albrecht, F., Gruhlke, M., Nwachukwu, I., and Slusarenko, A. (2014) Allicin: chemistry and biological properties. *Molecules* **19,** 12591–12618 CrossRef Medline
6. Sobolewska, D., Podolak, I., and Makowska-Wa?s, J. (2015) *Allium ursinum*: botanical, phytochemical and pharmacological overview. *Phytochem. Rev.* **14,** 81–97 CrossRef Medline
7. Kaschula, C., Hunter, R., and Parker, M. (2010) Garlic-derived anticancer agents: structure and biological activity of ajoene. *BioFactors* **36,** 78–85 CrossRef Medline
8. Blumenthal, M., Goldberg, A., and Brinckmann, J. (2000) Garlic in *Herbal Medicine*, pp. 130–133, American Botanical Council, Austin, TX
9. Slusarenko, A., Patel, A., and Portz, D. (2020) Control of Plant Diseases by Natural Products: Allicin from Garlic as a Case Dtudy in *Sustainable Disease Management in a European Context*, pp. 313–322, Springer, New York, NY
10. Block, E., Naganathan, S., Putman, D., and Zhao, S. (1993) Organosulfur chemistry of garlic and onion: recent results. *Pure Appl. Chem.* **65,** 625–632 CrossRef
11. Lanzotti, V. (2006) The analysis of onion and garlic. *J. Chromatogr. A* **1112,** 3–22 CrossRef Medline
12. Zhou, W., Liu, A., and Du, G. (2018) Allicin in *Natural Small Molecule Drugs from Plants*, pp. 569–579. Springer, Singapore
13. Granroth, B. (1970) Biosynthesis and decomposition of cysteine derivatives in onion and other *Allium* species. *Ann. Acad. Sci. Fenn. Chem.* **154,** 4–71
14. Yoshimoto, Y., and Saito, K. (2019) *S*-Alk(en)ylcysteine sulfoxides in the genus *Allium*: proposed biosynthesis, chemical conversion, and bioactivities. *J. Exp. Bot.* **70,** 4121–4137 CrossRef
15. Yoshimoto, Y., Onuma, M., Mizuno, S., Sugino, Y., Nakabayashi, R., Imai, S., Tsuneyoshi, T., Sumi, S., and Saito, K. (2015) Identification of a flavin-containing *S*-oxygenating monooxygenase involved in alliin biosynthesis in garlic. *Plant J.* **83,** 941–951 CrossRef Medline
16. Reeder, R., and Sobrado, P. (2013) Flavin-dependent monooxygenases in siderophore biosynthesis in *Handbook of Flavoproteins*, Vol. 2, pp. 29–72, De Gruyter, Berlin, Germany
17. Huijbers, M., Montersino, S., Westphal, A., Tischler, D., and van Berkel, W. (2014) Flavin dependent monooxygenases. *Arch. Biochem. Biophys.* **544,** 2–17 CrossRef Medline
18. van Berkel, W., Kamerbeek, N., and Fraaije, M. (2006) Flavoprotein monooxygenases, a diverse class of oxidative biocatalysts. *J. Biotechnol.* **124,** 670–689 CrossRef Medline
19. Robinson, R., Badieyan, S., and Sobrado, P. (2013) C4a-hydroperoxyflavin formation in N-hydroxylating flavin monooxygenases is mediated by the 2′-OH of the nicotinamide ribose of $NADP^+$. *Biochemistry* **52,** 9089–9091 CrossRef
20. Abdelwahab, H., Martin Del Campo, J. S., Dai, Y., Adly, C., El-Sohaimy, S., and Sobrado, P. (2016) Mechanism of rifampicin inactivation in *Nocardia farcinica*. *PLoS ONE* **11,** e0162578 CrossRef Medline
21. Catucci, G., Gao, C., Sadeghi, S., and Gilardi, G. (2017) Chemical applications of class B flavoprotein monooxygenases. *Rend. Lincei* **28,** 195–206 CrossRef
22. Schlaich, N. (2007) Flavin-containing monooxygenases in plants: looking beyond detox. *Trends Plant Sci.* **12,** 412–418 CrossRef Medline
23. Hartman, M., Zeier, T., Bernsdorff, F., Reichel-Deland, V., Kim, D., Hohmann, M., Scholten, N., Schuck, S., Bräutigam, A., Hölzel, T., Ganter, C., and Zeier, J. (2018) Flavin monooxygenase-generated *N*-hydroxypipecolic acid is a critical element of plant systemic immunity. *Cell* **173,** 456–469 CrossRef Medline
24. Dai, X., Mashiguchi, K., Chen, Q., Kasahara, H., Kamiya, Y., Ojha, S., DuBois, J., Ballou, D., and Zhao, Y. (2013) The biochemical mechanism of auxin biosynthesis by an arabidopsis YUCCA flavin-containing monooxygenase. *J. Biol. Chem.* **288,** 1448–1457 CrossRef Medline
25. Wojcieszyńska, D., Hupert-Kocurek, K., and Guzik, U. (2012) Flavin-dependent enzymes in cancer prevention. *Int. J. Mol. Sci.* **13,** 16751–16768 CrossRef Medline
26. Kong, W., Li, J., Yu, Q., Cang, W., Xu, R., Wang, Y., and Ji, W. (2016) Two novel flavin-containing monooxygenases involved in biosynthesis of aliphatic glucosinolates. *Front. Plant Sci.* **7,** 1292 CrossRef Medline
27. Li, J., Hansen, B., Ober, J., Kliebenstein, D., and Halkier, B. (2008) Subclade of flavin-monooxygenases involved in aliphatic glucosinolate biosynthesis. *Plant Physiol.* **148,** 1721–1733 CrossRef Medline
28. Hansen, B., Kliebenstein, D., and Halkier, B. (2007) Identification of a flavin-monooxygenase as the S-oxygenating enzyme in aliphatic glucosinolate biosynthesis in *Arabidopsis*. *Plant J.* **50,** 902–910 CrossRef Medline
29. Franceschini, S., Fedkenheuer, M., Vogelaar, N., Robinson, R., Sobrado, P., and Mattevi, A. (2012) Structural insight into the mechanism of oxygen activation and substrate selectivity of flavin-dependent *N*-hydroxylating monooxygenases. *Biochemistry* **51,** 7043–7045 CrossRef Medline
30. Binda, C., Robinson, R., Martin Del Campo, J., Keul, N., Rodriguez, P., Robinson, H., Mattevi, A., and Sobrado, P. (2015) An unprecedented NADPH domain conformation in lysine monooxygenase NbtG provides insights into uncoupling of oxygen consumption from substrate hydroxylation. *J. Biol. Chem.* **290,** 12676–12688 CrossRef Medline
31. Robinson, R., Rodriguez, P., and Sobrado, P. (2014) Mechanistic studies on the flavin-dependent N^6-lysine monooxygenase MbsG reveal an unusual control for catalysis. *Arch. Biochem. Biophys.* **550–551,** 58–66 CrossRef Medline
32. Siddens, L., Krueger, S., Henderson, M., and Williams, D. (2014) Mammalian flavin-containing monooxygenase (FMO) as a source of hydrogen peroxide. *Biochem. Pharmacol.* **89,** 141–147 CrossRef Medline
33. Hill, J., Coy, R., and Lewandowski, P. (1990) Oxidation of cysteine to cystine using hydrogen peroxide. *J. Chem. Educ.* **67,** 172 CrossRef
34. Krissinel, E., and Henrick, K. (2007) Inference of macromolecular assemblies from crystalline state. *J. Mol. Biol.* **372,** 774–797 CrossRef Medline
35. Krissinel, E., and Henrick, K. (2004) Secondary-structure matching (SSM), a new tool for fast protein structure alignment in three dimensions. *Acta Crystallogr. D Biol. Crystallogr.* **60,** 2256–2268 CrossRef Medline
36. Alfieri, A., Malito, E., Orru, R., Fraaije, M. W., and Mattevi, A. (2008) Revealing the moonlighting role of NADP in the structure of a flavin-containing monooxygenase. *Proc. Natl. Acad. Sci. U.S.A.* **105,** 6572–6577 CrossRef Medline
37. Cho, H. J., Cho, H. Y., Kim, K. J., Kim, M. H., Kim, S. W., and Kang, B. S. (2011) Structural and functional analysis of bacterial flavin-containing monooxygenase reveals its ping-pong-type reaction mechanism. *J. Struct. Biol.* **175,** 39–48 CrossRef Medline
38. Kubitza, C., Faust, A., Gutt, M., Gath, L., Ober, D., and Scheidig, A. J. (2018) Crystal structure of pyrrolizidine alkaloid N-oxygenase from the grasshopper *Zonocerus variegatus*. *Acta Crystallogr. D Struct. Biol.* **74,** 422–432 CrossRef Medline

39. Li, C. Y., Chen, X. L., Zhang, D., Wang, P., Sheng, Q., Peng, M., Xie, B. B., Qin, Q. L., Li, P. Y., Zhang, X. Y., Su, H. N., Song, X. Y., Shi, M., Zhou, B. C., Xun, L. Y., *et al.* (2017) Structural mechanism for bacterial oxidation of oceanic trimethylamine into trimethylamine *N*-oxide. *Mol. Microbiol.* **103,** 992–1003 CrossRef Medline
40. Eswaramoorthy, S., Bonanno, J. B., Burley, S. K., and Swaminathan, S. (2006) Mechanism of action of a flavin-containing monooxygenase. *Proc. Natl. Acad. Sci. U.S.A.* **103,** 9832–9837 CrossRef Medline
41. Thodberg, S., and Jakobsen Neilson, E. (2020) The "green" FMOs: diversity, functionality and application of plant flavoproteins. *Catalysts* **10,** 329 CrossRef
42. Jones, M., Hughes, J., Tregova, A., Milne, J., Tomsett, B., and Collin, H. (2004) Biosynthesis of the flavour precursors of onion and garlic. *J. Exp. Bot.* **55,** 1903–1918 CrossRef Medline
43. Kim, N., Park, M., Jang, F., and Lee, J. (2011) Volatile distribution in garlic (*Allium sativum L.)* by solid phase microextraction (SPME) with different processing conditions. *Food Sci. Biotechnol.* **20,** 775–782 CrossRef
44. Molina-Calle, M., Priego-Capote, F., and Luque de Castro, M. (2017) Headspace GC-MS volatile profile of black garlic vs fresh garlic: evolution along fermentation and behavior under heating. *LWT* **80,** 98–105 CrossRef
45. Nurlidia, M., Herng, H. J., Samsudin, S. J., Sufian, S., and Uemura, Y. (2016) Quantification and characterization of allicin in garlic extract. *J. Med. Biol. Eng.* **5,** 24–27 CrossRef
46. González-Morales, S., Pérez-Labrada, F., García-Enciso, E., Leija-Martínez, P., Medrano-Macías, J., Dávila-Rangel, I., Juárez-Maldonado, A., Rivas-Martínez, E., and Benavides-Mendoza, A. (2017) Selenium and sulfur to produce allium functional crops. *Molecules* **22,** 558 CrossRef
47. Chhabrie, S., and Desai, K. (2014) Sulphur metabolism of garlic: integrating complexity of flavour precursors. *Helix* **3,** 541–545
48. Noji, M., and Saito, K. (2003) Sulphur amino acids: biosynthesis of cysteine and methionine in *Sulphur in Plants*, pp. 135–144, Springer, Berlin, Germany
49. Shih, W., Chang, C., Chen, H., and Fan, K. (2018) Antioxidant activity and leukemia initiation prevention *in vitro* and *in vivo* by *N*-acetyl-L-cysteine. *Oncol. Lett.* **16,** 2046–2052 CrossRef Medline
50. Yamaguchi, Y., and Kumagai, H. (2020) Characteristics, biosynthesis, decomposition, metabolism and functions of the garlic odour precursor, *S*-allyl-L-cysteine sulfoxide. *Exp. Ther. Med.* **19,** 1528–1535 CrossRef
51. Keusgen, M. (2008) Unusual cystine lyase activity of the enzyme alliinase: direct formation of polysulphides. *Planta Med.* **74,** 73–79 CrossRef Medline
52. Ballou, D., and Entsch, B. (2013) The Reaction Mechanisms of Groups A and B Flavoprotein Monooxygenases in *Handbook of Flavoproteins*, Vol. 2, pp. 1–28, Walter de Gruyter, Berlin, Germany
53. Wijker, R., Pati, S., Zeyer, J., and Hofstetter, T. (2015) Enzyme kinetics of different types of flavin-dependent monooxygenases determine the observable contaminant stable isotope fractionation. *Environ. Sci. Technol. Lett.* **2,** 329–334 CrossRef
54. Palfey, B., and McDonald, C. (2010) Control of catalysis in flavin-dependent monooxygenases. *Arch. Biochem. Biophys.* **493,** 26–36 CrossRef Medline
55. Romero, E., Fedkenheuer, M., Chocklett, S., Qi, J., Oppenheimer, M., and Sobrado, P. (2012) Dual role of NADP(H) in the reaction of a flavin dependent *N*-hydroxylating monooxygenase. *Biochim. Biophys. Acta* **1824,** 850–857 CrossRef Medline
56. Dhatwalia, R., Singh, H., Solano, L. M., Oppenheimer, M., Robinson, R. M., Ellerbrock, J. F., Sobrado, P., and Tanner, J. J. (2012) Identification of the NAD(P)H binding site of eukaryotic UDP-galactopyranose mutase. *J. Am. Chem. Soc.* **134,** 18132–18138 CrossRef Medline
57. Dhatwalia, R., Singh, H., Oppenheimer, M., Karr, D. B., Nix, J. C., Sobrado, P., and Tanner, J. J. (2012) Crystal structures and small-angle X-ray scattering analysis of UDP-galactopyranose mutase from the pathogenic fungus *Aspergillus fumigatus*. *J. Biol. Chem.* **287,** 9041–9051 CrossRef
58. Chocklett, W., and Sobrado, P. (2010) *Aspergillus fumigatus* SidA is a highly specific ornithine hydroxylase with bound flavin cofactor. *Biochemistry* **49,** 6777–6783 CrossRef Medline
59. Fabiani, A., Versari, A., Parpinello, G., Castellari, M., and Galassi, S. (2002) High-performance liquid chromatographic analysis of free amino acids in fruit juices using derivatization with 9-fluorenylmethyl-chloroformate. *J. Chromatogr. Sci.* **40,** 14–18 CrossRef
60. Kumar, M., and Farmer, P. (2017) Trapping reactions of the sulfenyl and sulfinyl tautomers of sulfenic acids. *ACS Chem. Biol.* **12,** 474–478 CrossRef Medline
61. Alcock, L., Oliveira, B., Deery, M., Jones, G., Tierney, M., Kramer, H., Pukala, T., Bernardes, G., Perkins, M., and Chalker, J. (2019) Norbornene probes for the detection of cysteine sulfenic acid in cells. *ACS Chem. Biol.* **14,** 594–598 CrossRef Medline
62. Valentino, H., and Sobrado, P. (2019) Performing anaerobic stopped-flow spectrophotometry inside of an anaerobic chamber. *Methods Enzymol.* **620,** 51–88
63. Kabsch, W. (2010) XDS. *Acta Crystallogr. D Biol. Crystallogr.* **66,** 125–132 CrossRef Medline
64. Evans, P. R., and Murshudov, G. N. (2013) How good are my data and what is the resolution? *Acta Crystallogr. D Biol. Crystallogr.* **69,** 1204–1214 CrossRef Medline
65. Matthews, B. W. (1968) Solvent content of protein crystals. *J. Mol. Biol.* **33,** 491–497 CrossRef Medline
66. Schneider, T. R., and Sheldrick, G. M. (2002) Substructure solution with SHELXD. *Acta Crystallogr. D Biol. Crystallogr.* **58,** 1772–1779 CrossRef Medline
67. Zwart, P. H., Afonine, P. V., Grosse-Kunstleve, R. W., Hung, L. W., Ioerger, T. R., McCoy, A. J., McKee, E., Moriarty, N. W., Read, R. J., Sacchettini, J. C., Sauter, N. K., Storoni, L. C., Terwilliger, T. C., and Adams, P. D. (2008) Automated structure solution with the PHENIX suite. *Methods Mol. Biol.* **426,** 419–435 CrossRef Medline
68. Emsley, P., Lohkamp, B., Scott, W. G., and Cowtan, K. (2010) Features and development of Coot. *Acta Crystallogr. D Biol. Crystallogr.* **66,** 486–501 CrossRef Medline
69. Afonine, P. V., Grosse-Kunstleve, R. W., Echols, N., Headd, J. J., Moriarty, N. W., Mustyakimov, M., Terwilliger, T. C., Urzhumtsev, A., Zwart, P. H., and Adams, P. D. (2012) Towards automated crystallographic structure refinement with phenix.refine. *Acta Crystallogr. D Biol. Crystallogr.* **68,** 352–367 CrossRef Medline
70. Chen, V. B., Arendall, W. B., III, Headd, J. J., Keedy, D. A., Immormino, R. M., Kapral, G. J., Murray, L. W., Richardson, J. S., and Richardson, D. C. (2010) MolProbity: all-atom structure validation for macromolecular crystallography. *Acta Crystallogr. D Biol. Crystallogr* **66,** 12–21 CrossRef Medline
71. Gore, S., Sanz Garcia, E., Hendrickx, P. M. S., Gutmanas, A., Westbrook, J. D., Yang, H., Feng, Z., Baskaran, K., Berrisford, J. M., Hudson, B. P., Ikegawa, Y., Kobayashi, N., Lawson, C. L., Mading, S., Mak, L., *et al.* (2017) Validation of structures in the Protein Data Bank. *Structure* **25,** 1916–1927 CrossRef Medline
72. Liebschner, D., Afonine, P. V., Moriarty, N. W., Poon, B. K., Sobolev, O. V., Terwilliger, T. C., and Adams, P. D. (2017) Polder maps: improving OMIT maps by excluding bulk solvent. *Acta Crystallogr. D Struct. Biol* **73,** 148–157 CrossRef Medline